# Magnetic anisotropy in the Kitaev model systems $Na_2IrO_3$ and $RuCl_3$

Jiří Chaloupka[1,2] and Giniyat Khaliullin[3]

[1]*Central European Institute of Technology, Masaryk University, Kamenice 753/5, 62500 Brno, Czech Republic*

[2]*Department of Condensed Matter Physics, Faculty of Science, Masaryk University, Kotlářská 2, 61137 Brno, Czech Republic*

[3]*Max Planck Institute for Solid State Research, Heisenbergstrasse 1, D-70569 Stuttgart, Germany*

(Received 19 July 2016; revised manuscript received 10 August 2016; published 31 August 2016)

We study the ordered moment direction in the extended Kitaev-Heisenberg model relevant to honeycomb lattice magnets with strong spin-orbit coupling. We utilize numerical diagonalization and analyze the exact cluster ground states using a particular set of spin-coherent states, obtaining thereby quantum corrections to the magnetic anisotropy beyond conventional perturbative methods. It is found that the quantum fluctuations strongly modify the moment direction obtained at a classical level and are thus crucial for a precise quantification of the interactions. The results show that the moment direction is a sensitive probe of the model parameters in real materials. Focusing on the experimentally relevant zigzag phases of the model, we analyze the currently available neutron-diffraction and resonant x-ray-diffraction data on $Na_2IrO_3$ and $RuCl_3$ and discuss the parameter regimes plausible in these Kitaev-Heisenberg model systems.

DOI: 10.1103/PhysRevB.94.064435

## I. INTRODUCTION

Due to their intermediate spatial extension, $d$ electrons in transition-metal compounds comprise both the localized and itinerant features. This duality is manifested in a rich variety of metal-insulator transitions [1,2]. Even deep in the Mott-insulating phase, the $d$ electrons partially retain their kinetic energy, by making virtual hoppings to the neighboring sites and forming the covalent bonds. The internal structure of these bonds is dictated by the orbital shape of $d$ electrons as well as by Pauli principle and Hund's interactions among spins. This results in an intimate link between the nature of chemical bonds ("orbital order") and magnetism [3], which can be cast in terms of phenomenological Goodenough-Kanamori rules.

The Kugel-Khomskii models [4] form a theoretical framework where the "spin physics" and "orbital chemistry" are treated on equal footing. A special feature of these models is that the $d$ orbital is spatially anisotropic and hence cannot satisfy all the bonds simultaneously. In high-symmetry crystals, this results in a picture of fluctuating orbitals [5,6], where the frustration among different covalent bonds is resolved by virtue of their quantum superposition, lifting the orbital degeneracy without a static order.

It might seem that a relativistic spin-orbit coupling, which lifts the orbital degeneracy already on a single ion level [3,4], will readily eliminate the orbital frustration problem. This coupling does indeed greatly reduce the initially large spin-orbital Hilbert space of $d$ ions, leaving often just a twofold degenerate Kramers level with an effective ("pseudo") spin one-half [7]. It turns out, however, that the pseudospins still well "remember" the orbital frustration, by inheriting the bond-directional nature of orbital interactions via the spin-orbit entanglement [6].

The bond-directional nature of pseudospin interactions has profound consequences for magnetism (as well as for the properties of doped systems [8]). The most remarkable example, pointed out in Ref. [9], is a possible realization of Kitaev's honeycomb model [10] in materials with the $d^5(t_{2g})$ electronic configuration such as $Na_2IrO_3$. This theoretical proposal has sparked a broad interest in honeycomb lattice pseudospin systems (see the recent review paper [11] and references therein).

There is a direct experimental evidence [12] that the Kitaev-type interactions are indeed dominant in $Na_2IrO_3$. Unusual features pointing towards the Kitaev model have been observed [13] also in spin excitation spectra of $RuCl_3$ (this compound was suggested [14] to host pseudospin physics, too). On the other hand, it is also clear that there are terms in the pseudospin Hamiltonian that take these systems away from the Kitaev spin-liquid phase window [15]. The identification of these "undesired" interactions and clarification of their dependence on material parameters is an important issue that has been in the focus of many recent studies.

Experimentally, the strength of a dominant Kitaev coupling $|K|$ can readily be evaluated from an overall bandwidth of spin excitations; however, the determination of its sign and quantification of the subdominant terms is not straightforward and needs a theory support. The aim of this paper is to show that the direction of the ordered moments, which can be extracted from the neutron-diffraction and x-ray-diffraction data, contains valuable information on the model parameters, including the sign of $K$. Considering a symmetry dictated form of the model Hamiltonian, we calculate the pseudospin direction fully including quantum fluctuations which are expected to be crucial in frustrated spin models. We will point out that the pseudospin itself is not directly probed by neutrons; rather, they detect the direction of the *magnetic* moment which is not the same as that of the pseudospin. Similarly, we will describe how to extract the pseudospin direction from resonant x-ray-scattering (RXS) data.

The paper is organized as follows. Section II introduces the model Hamiltonian. Section III briefly discusses the pseudospin easy axis direction on a classical level. Section IV introduces the method of deriving the moment direction from exact diagonalization (ED) data. Section V presents the ED results on moment direction as a function of model parameters. Section VI considers a relation between the pseudospins and magnetic moments probed by neutron-diffraction and RXS experiments, and discusses implications of the theory for

 

$Na_2IrO_3$ and $RuCl_3$. Appendix A compares the method of Sec. IV with the standard approach. Appendix B derives the equations used in the analysis of RXS data. Finally, Appendix C discusses how the trigonal field can be extracted from $J = 3/2$ magnetic excitation spectra.

## II. EXTENDED KITAEV-HEISENBERG MODEL

To describe the interactions among the pseudospins (referred to as "spins" below), we adopt a model containing all symmetry allowed nearest-neighbor (NN) terms and the longer-range Heisenberg interactions:

$$\mathcal{H} = \sum_{\langle ij\rangle\in \mathrm{NN}} \mathcal{H}_{ij}^{(\gamma)} + \sum_{\langle ij\rangle\notin \mathrm{NN}} J_{ij}\boldsymbol{S}_i\cdot\boldsymbol{S}_j. \tag{1}$$

The nearest-neighbor contribution is the extended Kitaev-Heisenberg model [16–18] that, apart from the Heisenberg interaction, includes all the bond-anisotropic interactions compatible with the symmetries of a trigonally distorted honeycomb lattice. Its $z$-bond contribution (see Fig. 1 for the definitions of the bonds and spin axes) takes the following form:

$$\begin{aligned}\mathcal{H}_{ij}^{(z)} = {} & K\,S_i^zS_j^z + J\,\boldsymbol{S}_i\cdot\boldsymbol{S}_j + \Gamma\left(S_i^xS_j^y + S_i^yS_j^x\right)\\ & + \Gamma'\left(S_i^xS_j^z + S_i^zS_j^x + S_i^yS_j^z + S_i^zS_j^y\right).\end{aligned} \tag{2}$$

The Hamiltonian contributions for the other bonds ($x$ and $y$) are obtained by a cyclic permutation among $S_x, S_y, S_z$. The resulting alternation of the local easy axis directions from bond to bond, imposed by the Ising-like term $K$, brings about a strong frustration which, as discussed above, can be traced back to the orbital frustration problem in Kugel-Khomskii type models. An extensive discussion of the above Hamiltonian and its nontrivial symmetry properties can be found in Ref. [19].

With the Kitaev-coupling $K$ alone, the model has a spin-liquid ground state. Both $Na_2IrO_3$ and $RuCl_3$ show spin order where the zigzag-type ferromagnetic (FM) chains, running along the $a$ direction, are coupled to each other antiferromagnetically [see Fig. 1(b)]. This order becomes a ground state of the Kitaev model with $K > 0$ [antiferromagnetic (AF) sign], when a small FM $J < 0$ Heisenberg coupling is added [20]. If the Kitaev coupling is negative, $K < 0$ (FM sign), then zigzag order emerges due to longer-range AF couplings [21,22] and/or $\Gamma, \Gamma'$ terms [17–19]. Given that the stability of the Kitaev-liquid phase against perturbations strongly depends on the sign of $K$ [20], which scenario is realized in a given compound becomes an important issue.

Leaving aside the "orbital chemistry" aspects that decide the sign of $K$ as well as the other model parameters, we just mention that various *ab initio* estimates (see, e.g., [16,23,24]) generally support the FM $K < 0$ regime, most likely reflecting the decisive role of Hund's coupling effect on $K$ emphasized earlier [9,15]. However, we take here a phenomenological approach, considering the model with free parameter values including both signs of $K$. The $J$, $\Gamma$, and $\Gamma'$ values are varied such that the ground state stays within the zigzag phase. Based on a recent result [24] that third-NN Heisenberg coupling $J_3$ is more significant than second-NN $J_2$ in both $Na_2IrO_3$ and $RuCl_3$, we replace $J_{ij}$ in Eq. (1) by $J_3$, reducing thereby the parameter space.

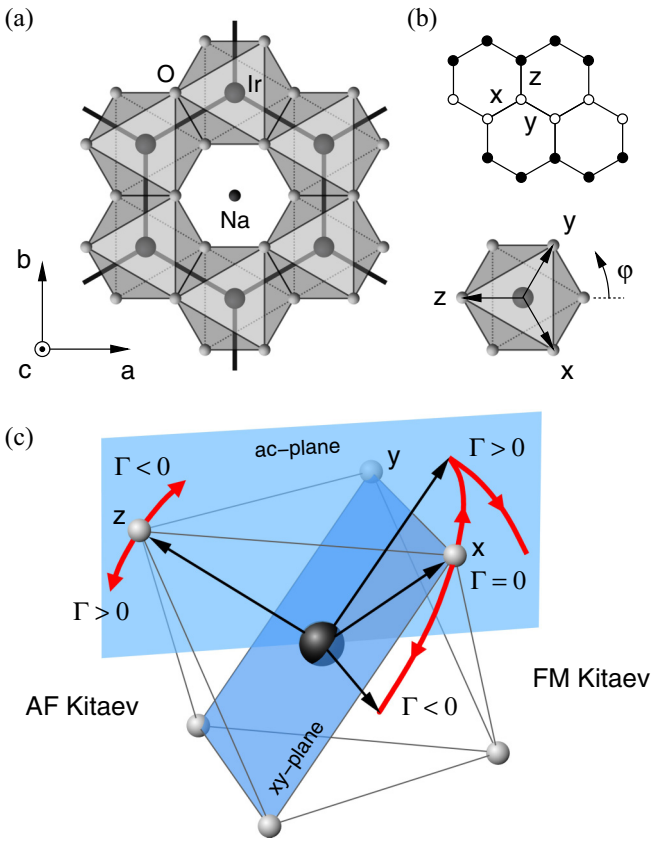


FIG. 1. (a) Top view of the honeycomb lattice of the edge-shared $IrO_6$ octahedra in $Na_2IrO_3$. (b) Three types of bonds and zigzag-AF state where $x$ and $y$ bonds connecting similar dots are FM, while the $z$ bonds are AF (top), and the orientation of the cubic axes $x, y, z$ with respect to the octahedra (bottom). (c) The possible directions of the ordered moment in the above zigzag state. In the AF Kitaev case the moment is tied to the cubic $z$ axis and deviates from it only slightly with nonzero $\Gamma$. In the FM Kitaev case with $\Gamma = 0$, it is constrained to the $xy$ plane classically, and pinned to a cubic $x$ or $y$ axis when quantum fluctuations are included. Nonzero $\Gamma < 0$ gradually pushes the moment direction towards the $b$ axis in the honeycomb plane, while positive $\Gamma$ drives it first towards the $ac$ plane [which is reached at $\Gamma \approx 0.05|K|$, see Fig. 3(a)], and then rotates the moment within the $ac$ plane towards the $a$ axis.

The magnetic anisotropy in the present model is a nontrivial problem, since the leading term $K$ is anisotropic by itself, and, on top of this highly frustrated interaction, the other terms which eventually drive a magnetic order in real compounds have a strong impact on magnetic energy profile. As illustrated in Fig. 1(c) and discussed in detail below, the ordered moment direction is very sensitive to the model parameters, and it shows a qualitatively different behavior in case of FM and AF Kitaev couplings. We note that the "moment direction" in this figure refers to that of pseudospin; Sec. VI explains how it is related to the magnetic moments probed by neutron-diffraction and x-ray-diffraction experiments.

## III. CLASSICAL MOMENT DIRECTION

Let us briefly mention the results of a classical analysis (for details see Appendix B of Ref. [19]) assuming the zigzag order with antiferromagnetic $z$ bonds as shown in Fig. 1(b). On this level, the moment direction is determined solely by the anisotropy parameters $K$, $\Gamma$, and $\Gamma'$ and corresponds to the eigenvector of the matrix

$$M = \begin{pmatrix} 2K & -\Gamma + 2\Gamma' & \Gamma \\ -\Gamma + 2\Gamma' & 2K & \Gamma \\ \Gamma & \Gamma & 0 \end{pmatrix} \tag{3}$$

that has the lowest eigenvalue. This minimizes the anisotropic contribution in the classical energy per site of the zigzag phase, $E_{\rm class} = \frac{1}{8}(J - K - 3J_3) + \frac{1}{8}\boldsymbol{m}^T M \boldsymbol{m}$, where $\boldsymbol{m}$ is a unit vector. The dominant Kitaev interaction contributing by the diagonal terms makes the main choice—it prefers either the $xy$ plane (FM $K < 0$) or the $z$ axis (AF $K > 0$). The smaller $\Gamma$ and $\Gamma'$ terms lead to a finer selection of the ordered moment direction.

In the case of the zigzag order stabilized by AF $K > 0$ and FM $J < 0$, the ordered moment direction is close to the $z$ axis being slightly tilted in the $ac$ plane mainly by virtue of $\Gamma$ [see Fig. 1(c)].

The FM $K < 0$ case, where the zigzag order is stabilized by $\Gamma$ and $J_3$ terms, is more complex. With $\Gamma = \Gamma' = 0$, the entire $xy$ plane is degenerate on a classical level. Further selection depends on the sign of $\Gamma - 2\Gamma'$, with the positive and negative sign making the moment to jump into the $ac$ plane or the $b$ axis in the honeycomb plane, respectively. In the former case, an increasing $\Gamma$ further pushes the moment closer to the honeycomb plane. As it has been found earlier [15,25] and discussed below, the Kitaev term generates an additional magnetic anisotropy due to quantum and/or thermal fluctuations, pinning the moment direction to the cubic axes. This will turn the above jumps into a gradual rotation of the easy axis with changing $\Gamma$, along the path shown in Fig. 1(c).

## IV. EXTRACTION OF THE MOMENT DIRECTION FROM A CLUSTER GROUND STATE

To determine the ground state of the Hamiltonian (1) and obtain the moment direction as a function of model parameters more rigorously than in the previous perturbative methods, we have performed an exact diagonalization using a hexagon-shaped 24-site supercell covering the honeycomb lattice. This cluster is highly symmetric and compatible with all the hidden symmetries of the model [19] so that no bias induced by the cluster geometry is expected.

Since the cluster ground state does not spontaneously break the symmetry and corresponds to a superposition of all possible degenerate orderings, the identification of the ordered moment direction is not straightforward. One possibility is to evaluate the $3 \times 3$ correlation matrix $\langle S^\alpha_{-\boldsymbol{Q}} S^\beta_{\boldsymbol{Q}} \rangle$ $(\alpha,\beta = x,y,z)$ at the ordering vector $\boldsymbol{Q}$ and to take the direction of the eigenvector corresponding to its largest eigenvalue. Because of specific problems of this standard approach in the present context (see Appendix A for details), we have developed here another method that brings a more intuitive picture of the exact ground state by "measuring" the presence of the classical states with a varying moment direction. As a basic building block, we utilize the spin-$\frac{1}{2}$ coherent state

$$|\theta,\phi\rangle = \mathcal{R}_z(\phi)\mathcal{R}_y(\theta)|\uparrow\rangle = e^{-i\phi S^z} e^{-i\theta S^y}|\uparrow\rangle \tag{4}$$

that is fully polarized along the $(\theta,\phi)$ direction [26]. Here the cubic axes are used as a convenient reference frame and $\theta$ and $\phi$ are the conventional spherical angles. A spin-coherent state on the cluster is constructed as a direct product

$$|\Psi\rangle = \prod_{j=1}^{N} |\theta_j,\phi_j\rangle \tag{5}$$

with the unit vectors $\boldsymbol{m}_j = (\cos\phi\sin\theta, \sin\phi\sin\theta, \cos\theta)_j$ forming the desired pattern. In this fully polarized classical state $\langle\Psi|S^\alpha_i S^\beta_j|\Psi\rangle = \frac{1}{4} m^\alpha_i m^\beta_j$ and the energy $\langle\Psi|\mathcal{H}|\Psi\rangle$ is thus equal to the classical energy. We consider only collinear states of FM, AF, and zigzag type. For example, a FM state with the moment direction $(\theta,\phi)$ is explicitly expressed as

$$|\Psi\rangle = \prod_{j=1}^{N} \left(e^{-i\phi/2}\cos\tfrac{\theta}{2}\,|\uparrow\rangle_j + e^{+i\phi/2}\sin\tfrac{\theta}{2}\,|\downarrow\rangle_j\right). \tag{6}$$

By varying $\theta$ and $\phi$ and evaluating the overlap with the exact cluster ground state $|\mathrm{GS}\rangle$, we obtain the probability map $P(\theta,\phi) = |\langle\Psi|\mathrm{GS}\rangle|^2$. The ordered moment direction is then identified by locating the maxima of $P(\theta,\phi)$.

There is an intrinsic width of the peaks in $P(\theta,\phi)$ due to the nonzero overlap of the spin-coherent states, namely, $|\langle\Psi|\Psi'\rangle|^2 = \cos^{2N}(\frac{1}{2}\Omega)$, where $\Omega$ is the angle between the directions $(\theta,\phi)$ and $(\theta',\phi')$. This gives an approximate half width at half maximum of $\sqrt{2/N}$ (in terms of the angular distance from the maximum), evaluating to about 17° for $N = 24$. Despite this sizable intrinsic width, the ordered moment direction can be detected with a high accuracy (limited only by the accuracy of the ground-state vector), as we see below.

## V. MOMENT DIRECTION—EXACT DIAGONALIZATION RESULTS

### A. Testing the method: Nearly Heisenberg limit

Before discussing in detail the ordered moment direction in the zigzag phases, relevant for actual compounds $Na_2IrO_3$ and $RuCl_3$, let us demonstrate the above method by considering the Kitaev-Heisenberg model close to the Heisenberg limit, $|J| \gg |K|$, with both signs of $J$. In such a situation, the FM or AF order is established by the dominant isotropic interaction, while the anisotropic Kitaev interaction merely selects the easy axis direction via an order-from-disorder mechanism [27].

We start with the FM case $J < 0$. Figure 2(a) is the corresponding probability map obtained by the method of Sec. IV for $K/J = 0.2$. The probability is clearly peaked at the directions of the cubic axes attaining there the maximum value $P_{\rm max}$ slightly less than $\frac{1}{6}$. This is due to the cluster ground state being a superposition of six possible classical states and a small contribution of quantum fluctuations. The width of the peaks matches well the intrinsic width estimated in Sec. IV.

That the $K$ term favors cubic axes for the ordered moment follows also from simple analytical calculations. By treating the quantum fluctuations within second-order perturbation

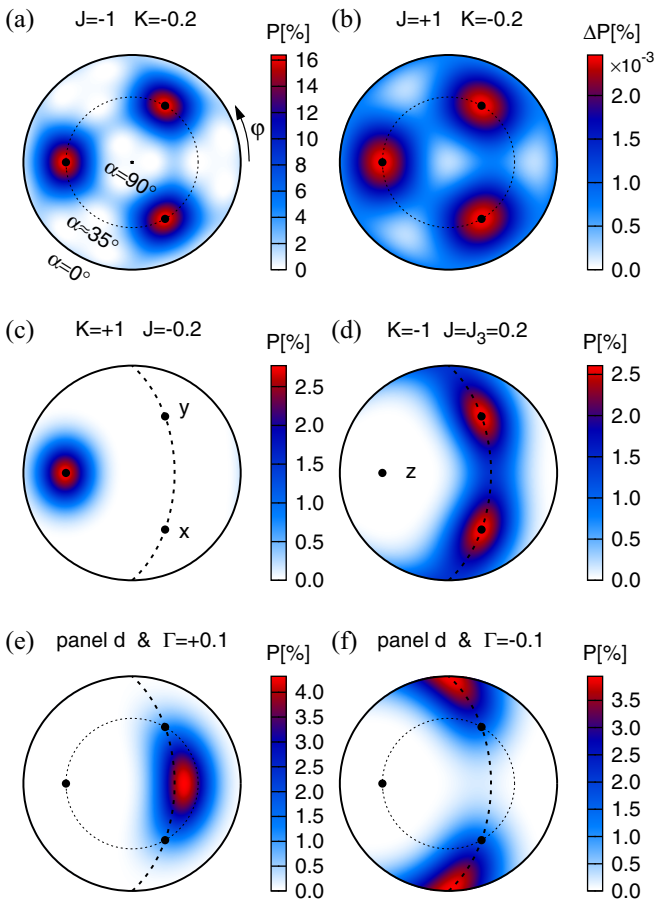


FIG. 2. (a) Map of the probability of the spin-coherent state given by Eq. (6) in the FM ground state of the KH model near the Heisenberg limit. The radial coordinate gives the angle $\alpha$ to the honeycomb plane; the polar angle $\varphi$ matches that defined in Fig. 1(b). (b) Probability map for the AF ground state obtained using small $K$ and dominant $J > 0$. Only the variation $\Delta P$ on top of $P_0 = 2.923\%$ is shown. (c) Probability map for the zigzag phase of the KH model with $K > 0$, $J < 0$ reveals a strong pinning to the $z$ axis. The coherent state corresponding to the zigzag pattern in Fig. 1(b) was used. Directions lying in the $xy$ plane are indicated by the dashed line. (d) Soft $xy$ plane for FM $K < 0$ zigzag stabilized by $J_3$. Cubic axes $x$ and $y$ are selected but the moment strongly fluctuates in the plane. (e,f) The same as in panel (d) but extended by a sizable $\Gamma$ term forcing the moment into the $ac$ plane (left) or the $b$ axis (right).

expansion (see Ref. [28] for details), we obtain the magnetic anisotropy energy

$$\delta E^{(2)}_{\rm FM} \approx \frac{K^2}{64|J|}\left(1 - m_x^4 - m_y^4 - m_z^4\right), \qquad (7)$$

depending on the moment direction given by a unit vector $\boldsymbol{m} = (m_x, m_y, m_z)$. This quantum correction on top of the isotropic classical energy is minimized for $\boldsymbol{m}$ pointing along the cubic axes $x, y$, and $z$ that become the easy axes, consistent with the ED result.

The case of the AF $J > 0$ is rather different due to the presence of large quantum fluctuations already in the Heisenberg limit. This is manifested in an almost flat probability profile with $P$ of about 3% [see Fig. 2(b)]. Nevertheless, the probability maxima again precisely locate the $x, y$, and $z$ directions for the ordered moments, consistent with the "order-from-disorder" calculations [15,25,28–30] in the models containing compass- or Kitaev-type bond-directional anisotropy.

### B. Moment direction in the zigzag phases

Having verified the method, we now move to the zigzag phases observed in $Na_2IrO_3$ and $RuCl_3$. We first inspect the case of $\Gamma, \Gamma' = 0$ when the anisotropy is due to the Kitaev term alone. Shown in Fig. 2(c) is the probability map for AF $K > 0$ and FM $J < 0$, where the $z$ axis is selected already on the classical level as discussed in Sec. III [31]. The probability is indeed strongly peaked at the direction of the $z$ axis. The small $P_{\rm max}$ of about 3% is again a signature of large quantum fluctuations in the ground state. Note that this number contains an overall reduction factor of $\frac{1}{6}$ due to the six possible zigzag states being superposed in the cluster ground state.

The probability map Fig. 2(d) for the FM $K < 0$ zigzag case reveals the moment being constrained to the vicinity of the $xy$ plane, as expected from classical considerations. Within this plane, the order-from-disorder mechanism selects the cubic axes $x$ and $y$ where the probability reaches its maxima. Concluding the survey of the probability maps, we show $P$ calculated including a large enough $\Gamma$ that leads to the selection of a direction within the $ac$ plane [$\Gamma > 0$, Fig. 2(e)] or the $b$ axis [$\Gamma < 0$, Fig. 2(f)].

The above three examples for the FM $K$ zigzag indicate a rather complex behavior of the moments in this case, as already suggested in Fig. 1(c). In the following, we therefore focus on the full $\Gamma$ dependence presented in Fig. 3(a) in the form of the angles $\alpha(\Gamma)$ (the angle to the honeycomb plane) and $\varphi(\Gamma)$ (polar angle of the projection into the honeycomb plane). Instead of the jump in $\alpha(\Gamma)$ obtained on a classical level, we find a finite window $|\Gamma| \lesssim 0.05|K|$ of an order-from-disorder stabilized phase, where the moment direction gradually moves from the cubic axis ($\Gamma = 0$) to either the $b$ axis ($\Gamma < 0$) or the $ac$ plane ($\Gamma > 0$). Once the critical value of $\Gamma$ is reached, the moment either stays along the $b$ axis or is pushed down within the $ac$ plane closer to the honeycomb plane. Figure 3(b) illustrates the evolution of $\alpha(\Gamma)$ for different values of $J_3$ stabilizing the zigzag order. For small $J_3$, the dominant directional Kitaev term makes the moment more pinned to the cubic axes, which is manifested by a significantly reduced slope of $\alpha(\Gamma)$ near $\Gamma = 0$ compared to the large-$J_3$ case. On the other hand, the critical values of $\Gamma$ are only slightly affected by $J_3$.

The above crossover behavior near $\Gamma = 0$ may be easily understood and even semiquantitatively reproduced by considering a competition of the classical energy and the order-from-disorder potential as follows. Keeping the moment $\boldsymbol{m} = (\cos\phi, \sin\phi, 0)$ within the $xy$ plane preferred by $K < 0$, we can evaluate the classical energy per site:

$$E_{\rm class} = \tfrac{1}{8}(K - 3J_3 + J) - \tfrac{1}{8}(\Gamma - 2\Gamma')\sin 2\phi. \qquad (8)$$

In this contribution, the anisotropy is due to the $\Gamma$ and $\Gamma'$ terms only. $E_{\rm class}$ is complemented by an order-from-disorder potential $E_{\rm fluct}(\phi)$ that should contain four equivalent minima at $\phi = 0, \frac{1}{2}\pi, \pi, \frac{3}{2}\pi$ corresponding to the cubic axes (supported by the $K$ term). Such a potential can be represented by the

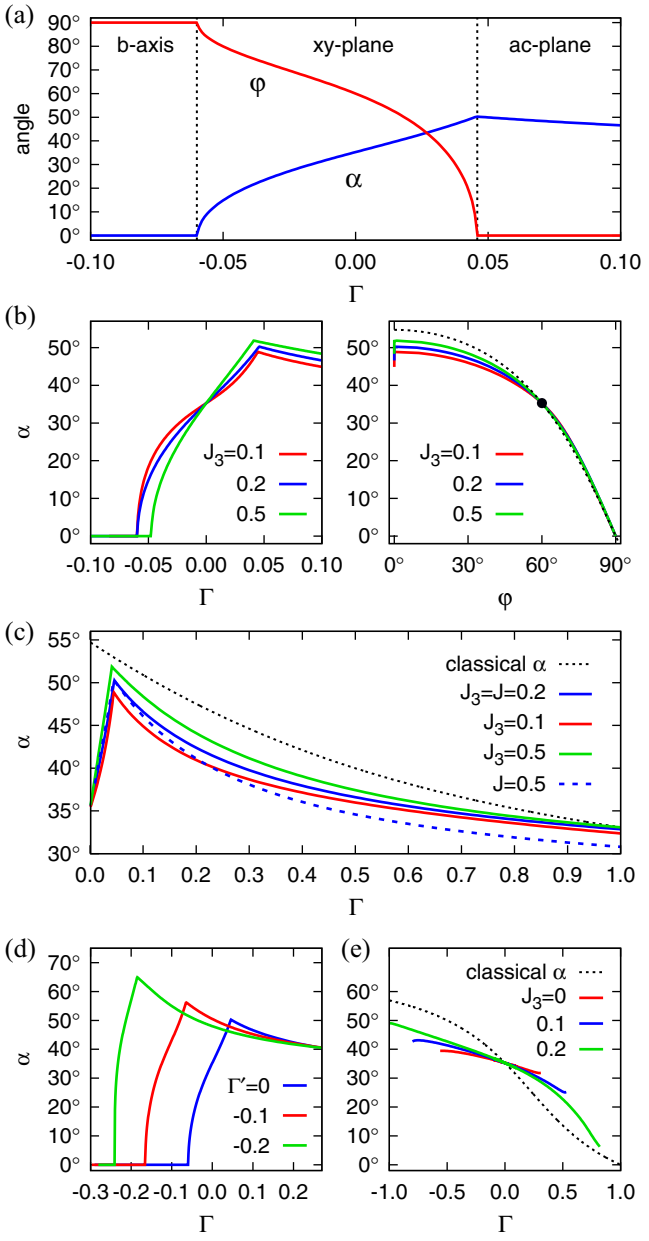


FIG. 3. (a) Γ-dependent angles $\alpha$, $\varphi$ specifying the moment direction reveal three regimes for FM $K$ zigzag supported by small $J_3$. The values $K=-1$ and $J=J_3=0.2$ were used. At $\Gamma=0$, the angles give the direction towards an oxygen ion. A crossover in the interval $|\Gamma| \lesssim 0.05$ corresponds to the path shown in Fig. 1(c). (b) Left panel shows the angle $\alpha$ for $K=-1$, $J=0.2$ and several $J_3$ values manifesting a stronger pinning to the cubic axis at smaller $J_3$. The same data are presented as $\alpha(\varphi)$ in the right panel together with $\alpha(\varphi)$ corresponding to the $xy$ plane (dashed). The black dot indicates the cubic axis direction. (c) The angle $\alpha$ for larger values of $\Gamma>0$ compared to the classical result of Ref. [19] (dotted). The blue solid curve is a continuation of that of panel (a), red and green curves are calculated using different $J_3$ values used in panel (b), and the blue dashed curve denotes a larger $J$ value. (d) The angle $\alpha$ for the parameters $K=-1$, $J=J_3=0.2$, and several $\Gamma'$ values. (e) Γ-dependent $\alpha$ in the AF $K=+1$ case with $J=-0.2$ and several $J_3$ values compared to the classical result of Ref. [19] (dotted). The endpoints of the curves are determined by a sharp drop of the probability of the classical zigzag state indicating a phase boundary.

following form:

$$E_{\text{fluct}} = V \sin^2 2\phi, \tag{9}$$

approximating $E_{\text{fluct}}(\phi)$ by its lowest harmonic. This function is characterized by a single unknown parameter—the barrier height $V$, determined mainly by the dominant $K$. Assuming $\Gamma'=0$, the minimization of the total energy $E_{\text{class}}+E_{\text{fluct}}$ gives $\phi(\Gamma)=\frac{1}{2}\arcsin\frac{\Gamma}{16V}$ and the critical value $\Gamma_{\text{crit}}=16V$. This enables us to extract effective $V$ from our numerical data. By taking $\Gamma_{\text{crit}}\approx 0.05|K|$ observed in Figs. 3(a) and 3(b) we get $V\approx 0.003|K|$. Furthermore, converting $\phi$ in the $xy$ plane to the angle $\alpha$ to the honeycomb plane, we obtain "phenomenological" $\alpha(\Gamma)=\arcsin\sqrt{\frac{1}{3}(1+\frac{\Gamma}{16V})}$ that roughly approximates the numerical $\alpha(\Gamma)$ data. The agreement between these two $\alpha(\Gamma)$ profiles improves with increasing $J_3$, when the order-from-disorder potential becomes more harmonic and the deviation of the moment direction from the $xy$ plane for $\Gamma>0$ reduces [see Fig. 3(b)]. In fact, Eqs. (8) and (9), together with the value of $V\approx 0.003|K|$ extracted from the ED data, may be used for a semiquantitative determination of the easy axis direction within the $xy$ plane.

For curiosity, we have evaluated the potential barrier $V$ also analytically, by two slightly different methods. First, as in Sec. V A, we estimated quantum corrections for the zigzag phase along the lines of Ref. [28]. This reproduced the above form (9) of the anisotropy potential, and provided a consistent estimate of $V\approx 0.005|K|$. An alternative evaluation of the anisotropy potential within the linear spin-wave framework resulted in zero-point energy of the same form as Eq. (9) again, but with an overestimated value of $V\approx 0.014|K|$.

In $Na_2IrO_3$ the moment direction was found [12] in the $ac$ plane suggesting that $\Gamma>\Gamma_{\text{crit}}$ for this material. We thus focus on this particular case and investigate how the precise value of $\alpha$ is affected by the model parameters in more detail. Already on a classical level, finite $\Gamma>0$ rotates the moment within the $ac$ plane from $\alpha\approx 54.7^\circ$ (corresponding to the $xy$ plane) toward the honeycomb plane ($\alpha=0$). Such an effect is well visible also in Figs. 3(a) and 3(b). Presented in Fig. 3(c) are a few representative $\alpha(\Gamma)$ curves for larger values of $\Gamma$ up to $|K|$ that serve as a test of the classical prediction

$$\tan 2\alpha = 4\sqrt{2}\,\frac{1+r}{7r-2} \quad \text{with} \quad r=-\frac{\Gamma}{K+\Gamma'} \tag{10}$$

derived in Ref. [19]. As we find, the quantum fluctuations included in the exact ground state push the ordered moments much closer to the honeycomb plane. The difference is substantial and needs to be considered when trying to quantify the model parameters based on the experimental data.

So far, we have considered $\Gamma'=0$ only, while a small negative $\Gamma'$ is expected to be generated by a trigonal compression [18,19,32]. Based on Eq. (8), $\Gamma'$ is expected to effectively shift the value of $\Gamma$ in the first approximation. Indeed, as shown in Fig. 3(d), the rough three-phase picture as in Fig. 3(a) is preserved and the negative $\Gamma'$ shifts the $\alpha(\Gamma)$ curve in the negative direction. This enables $\alpha$ to reach higher values, even above the $xy$-plane angle $54.7^\circ$.

Finally, in Fig. 3(e) we briefly analyze the AF $K$ situation with the moment near the $z$ axis. In contrast to the FM $K$ case, small $\Gamma$ has a relatively little effect here, because the $z$ axis

is classically selected by the dominant $K > 0$ itself. Quantum fluctuations are found to generate an even stronger pinning to the $z$ axis, compared to the classical solution of Ref. [19]. Only a very large $\Gamma$ coupling is able to take the spin away from the $z$ axis.

## VI. COMPARISON TO EXPERIMENT

### A. Extracting pseudospin direction from resonant x-ray and neutron-scattering data

Having quantified the pseudospin easy axis direction as a function of the Hamiltonian parameters, we consider now how this "pseudomoment" direction is related to that of real magnetic moments measured by neutron-scattering and x-ray scattering experiments. To this end, we first define the pseudospin one-half wave functions including crystal field of trigonal symmetry. The latter splits the $t_{2g}$ manifold into an orbital singlet $a_{1g} = \frac{1}{\sqrt{3}}(xy + yz + zx)$ and the $e'_g$ doublet $\{\frac{1}{\sqrt{6}}(yz + zx - 2xy)\,;\, \frac{1}{\sqrt{2}}(zx - yz)\}$. Denoting this splitting by $\Delta$ and using the hole representation, we have

$$H = \Delta\, \tfrac{1}{3}[2n(a_{1g}) - n(e'_g)]. \tag{11}$$

Within a point-charge model, positive (negative) $\Delta$ would correspond to a compression (elongation) of octahedra along the trigonal $c$ axis. The actual value of $\Delta$ in real material is decided by various factors, but this issue is not relevant in the present context.

In terms of the effective angular momentum $l = 1$ of the $t_{2g}$ shell, the $a_{1g}$ state corresponds to the $l_c = 0$ state, while the $e'_g$ doublet hosts the $l_c = \pm 1$ states, using the quantization axis $c$ suggested by the trigonal crystal field. Explicitly,

$$|0\rangle = \frac{1}{\sqrt{3}}(|yz\rangle + |zx\rangle + |xy\rangle), \tag{12}$$

$$|\pm 1\rangle = \pm\frac{1}{\sqrt{3}}(e^{\pm 2\pi i/3}|yz\rangle + e^{\mp 2\pi i/3}|zx\rangle + |xy\rangle). \tag{13}$$

Via these $l_c$ states, pseudospin-$\frac{1}{2}$ wave functions are defined as

$$\left|+\tfrac{1}{2}\right\rangle = +\sin\vartheta\,|0,\uparrow\rangle - \cos\vartheta\,|+1,\downarrow\rangle, \tag{14}$$

$$\left|-\tfrac{1}{2}\right\rangle = -\sin\vartheta\,|0,\downarrow\rangle + \cos\vartheta\,|-1,\uparrow\rangle, \tag{15}$$

where $\uparrow$ and $\downarrow$ refer to the projections of the hole spin on the trigonal $c$ axis. The spin-orbit "mixing" angle $0 \leqslant \vartheta \leqslant \pi/2$ is given by $\tan 2\vartheta = 2\sqrt{2}/(1+\delta)$, where $\delta = 2\Delta/\lambda$.

Using the wave functions (14) and (15), we may express the spin $\boldsymbol{s}$ and orbital $\boldsymbol{l}$ moments of a hole via the pseudospin $\boldsymbol{S}$. In a cubic limit, i.e., $\Delta = 0$, one has $\boldsymbol{s} = -\frac{1}{3}\boldsymbol{S}$, $\boldsymbol{l} = \frac{4}{3}\boldsymbol{S}$, and total magnetic moment $\boldsymbol{M} = (2\boldsymbol{s} - \boldsymbol{l}) = -2\boldsymbol{S}$ (note a negative $g$ factor $g = -2$). These relations imply that the pseudospin easy axis direction is identical to that of spin, orbital, and magnetic moments when the trigonal field is zero. However, this is no longer valid at finite $\Delta$. For instance, strong compression ($\vartheta = 0$) would completely suppress the $ab$-plane components of magnetic moments, so the pseudospin and magnetic moment will not be parallel anymore (unless pseudospin is ordered along the $c$ axis).

The x rays and neutrons couple initially to the spin and orbital moments, and the scattering operator has to be projected onto the pseudospin basis. We first consider an effective RXS operator. For pseudospin one-half in a trigonal field, it has to have a form $\hat{R} \propto i f_{ab}(P_a S_a + P_b S_b) + i f_c P_c S_c$, where $\boldsymbol{P} = \boldsymbol{\varepsilon} \times \boldsymbol{\varepsilon}'$ and $\boldsymbol{\varepsilon}$ ($\boldsymbol{\varepsilon}'$) is the polarization of the incoming (outgoing) photon. This can be written as $\hat{R} \propto i\,\boldsymbol{P}\cdot\boldsymbol{N}$, introducing a vector $\boldsymbol{N} = (f_a S_a, f_b S_b, f_c S_c)$ with $f_a = f_b \equiv f_{ab}$. The RXS data determine a direction of this auxiliary vector $\boldsymbol{N}$; in $Na_2IrO_3$, it was found to make an angle $\alpha_N \approx 44.3^\circ$ to the $ab$ plane [12]. However, this is not yet the pseudospin direction, since $f_{ab} \neq f_c$ and hence $\alpha_S \neq \alpha_N$, unless the trigonal field is exactly zero (unlikely in real materials). To access the pseudospin angle $\alpha_S$ and quantify the model parameters, one has to know the "RXS factors" $f_{ab}$ and $f_c$.

We have derived the $f$ factors (see Appendix B for details). For the $L_3$ edge, they read as

$$f_{ab} = \frac{1}{2} + \frac{5}{6\sqrt{2}}\, s_{2\vartheta} - \frac{1}{6}\, c_{2\vartheta}, \tag{16}$$

$$f_c = 1 + \frac{2}{3}\, c_{2\vartheta} - \frac{1}{3\sqrt{2}}\, s_{2\vartheta}. \tag{17}$$

Here, $s_{2\vartheta} = 2\sqrt{2}/r$, $c_{2\vartheta} = (1+\delta)/r$, and $r = \sqrt{8 + (1+\delta)^2}$. Figure 4(a) shows the $f$ factors as a function of trigonal field parameter $\delta$. In the cubic limit, one has $f_{ab} = f_c$ and hence $\boldsymbol{N}$ is parallel to $\boldsymbol{S}$, as expected.

For completeness, we show also the $f$ factors for the $L_2$ edge:

$$f_{ab} = 2 f_c = -\tfrac{3}{2} + \tfrac{1}{2}\, c_{2\vartheta} + \sqrt{2}\, s_{2\vartheta}, \tag{18}$$

which vanish at the $\delta = 0$ limit, as a consequence of the spin-orbit entangled nature of pseudospins [33].

In neutron-diffraction experiments, the magnetic moment $\boldsymbol{M} = (g_a S_a, g_b S_b, g_c S_c)$ is probed. For the pseudospins as defined above, the $g$ factors are (neglecting covalency effects [7])

$$g_{ab} = -(1 + \sqrt{2}\, s_{2\vartheta} - c_{2\vartheta}), \tag{19}$$

$$g_c = -(1 + 3\, c_{2\vartheta}). \tag{20}$$

The $g$-factor anisotropy can quantify the strength of the trigonal field, as illustrated in Fig. 4(b). Again, magnetic moment direction is in general different from that of pseudospin, and to access the latter one needs to know the $g$ factors.

These considerations imply that the orientations of the (x-ray) $\boldsymbol{N}$ vector and magnetic moment $\boldsymbol{M}$ differ from each other, and also from that of pseudospin $\boldsymbol{S}$ which enters the model Hamiltonian. As we show in Fig. 4(c), their relative angles come in the order $\alpha_M > \alpha_N > \alpha_S$ for positive $\Delta$, and in reversed order $\alpha_S > \alpha_N > \alpha_M$ for negative $\Delta$. Ideally, having measured both $\boldsymbol{N}$ and $\boldsymbol{M}$ directions in the same compound, one could extract the crystal-field parameter $\delta$ using the above equations, and uniquely fix the pseudospin easy axis angle $\alpha_S$. In principle, the $g$-factor anisotropy provides the same information on $\delta$, but obtaining $g$ factors in magnetically concentrated systems is a somewhat nontrivial task. Alternatively, one could extract the value and sign of $\Delta$ directly from the splitting and anisotropy of the high-energy $J = 3/2$ quartet in single crystals (see Appendix C for details).

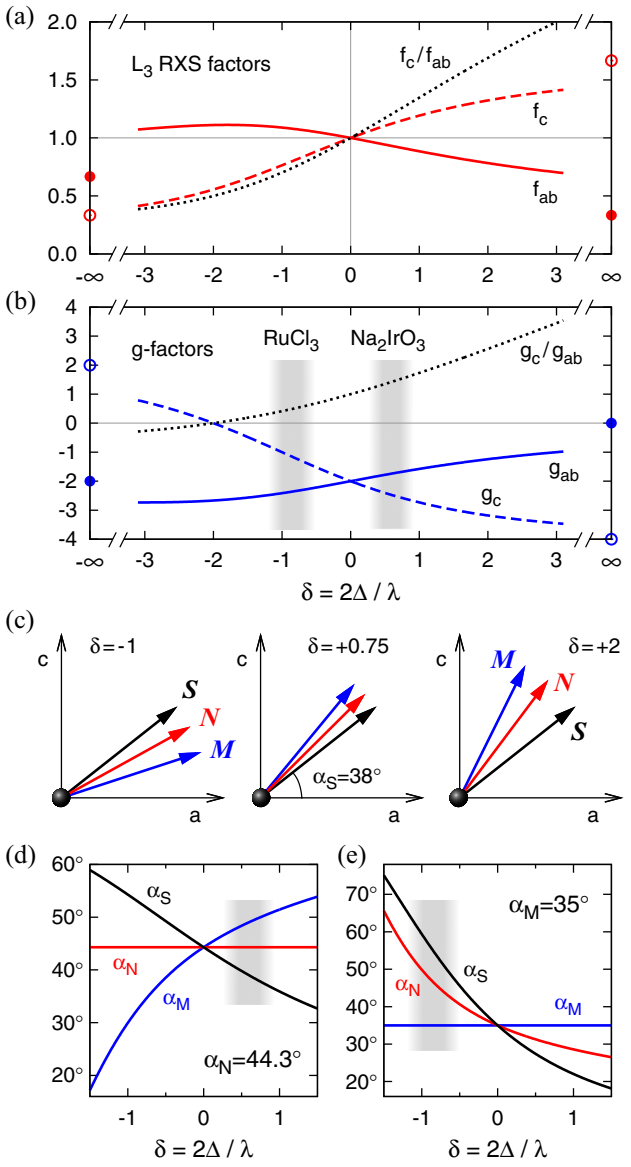


FIG. 4. (a) Factors $f$ entering the relation between the pseudospin $\boldsymbol{S}$ and $L_3$ RXS vector $\boldsymbol{N}$ presented as functions of the trigonal field. (b) $g$ factors as functions of the trigonal field. Intervals of $\delta$ consistent with the $g$ factors suggested by the experimental data on $RuCl_3$ [34,35] and $Na_2IrO_3$ [36,37] are indicated by shading. (c) Directions of the $\boldsymbol{S}$, $\boldsymbol{N}$, and $\boldsymbol{M}$ vectors for sample values of the trigonal field parameter $\delta$ and a fixed pseudospin angle $\alpha_S = 38^\circ$. The case with the negative $\delta = -1$ could be relevant for $RuCl_3$, while positive $\delta = +0.75$ with the reverse order of the vectors $\boldsymbol{M}$, $\boldsymbol{N}$, and $\boldsymbol{S}$ for $Na_2IrO_3$. (d),(e) Angles $\alpha_S$, $\alpha_N$, and $\alpha_M$ of the vectors $\boldsymbol{S}$, $\boldsymbol{N}$, and $\boldsymbol{M}$ to the honeycomb plane as functions of $\delta$ keeping fixed $\alpha_N = 44.3^\circ$ (d) or $\alpha_M = 35^\circ$ (e). The shaded $\delta$ intervals are the same as in panel (b).

### B. Implications for $Na_2IrO_3$ and $RuCl_3$

Armed with the above relations between different moments, and using the results of Sec. V B, let us now analyze the available experimental data on $Na_2IrO_3$ and $RuCl_3$.

Starting with the case of $Na_2IrO_3$, we utilize the value $\alpha_N \approx 44.3^\circ$ determined recently by RXS [12]. Keeping this experimental constraint, in Fig. 4(d) we plot the remaining angles $\alpha_M$ and $\alpha_S$ as functions of the relative strength of the trigonal crystal field $\delta$. In Ref. [19], the value $\Delta/\lambda \approx 3/8$ was deduced based on the splitting $\Delta_{BC} \approx 0.1$ eV of the $J = 3/2$ quartet [37]. As seen in Fig. 4(b), the corresponding $\delta \approx 0.75$ is also roughly consistent with the anisotropy of the $g$ factors, $g_c/g_{ab} \approx 1.4$, obtained by fitting the temperature-dependent magnetic susceptibilities $\chi_c > \chi_{ab}$ [36]. The data in Fig. 4(d) then suggest that the magnetic moment takes an angle of about $\alpha_M \approx 50^\circ$ to the honeycomb plane, while the pseudospin angle $\alpha_S$ is roughly 38–40°. Such a deviation of the pseudospin from the $xy$ plane ($\alpha \approx 54.7^\circ$) implies a sizable $\Gamma$ value. Based on Fig. 3(c) we may naively expect the $\Gamma/|K|$ ratio in the range 0.3–0.5. We emphasize, however, that this conclusion relies on the above estimate of the trigonal field, that should be verified by measuring the "magnetic" angle $\alpha_M$ directly by neutron scattering.

Compared to $Na_2IrO_3$, $RuCl_3$ shows an opposite magnetic anisotropy behavior with $\chi_c \ll \chi_{ab}$ [34]. The magnetic structure has been recently investigated by neutron scattering [38], with the result $\alpha_M \approx 35^\circ$ and $\varphi$ being equal to either 0 or 180°. Similarly to Fig. 4(d), in Fig. 4(e) we keep the measured angle, now $\alpha_M$, fixed at its experimental value, and plot $\alpha_S$ and $\alpha_N$ for varying $\delta = 2\Delta/\lambda$. This parameter could be obtained from the anisotropy of $J = 3/2$ transitions in single crystals (see Appendix C). We are not aware of such a direct measurement in $RuCl_3$, so the trigonal field is best assessed by considering the anisotropy of the $g$ factors. References [34,35] reported in-plane and out-of-plane magnetization curves measured for high fields up to 60 T. Even though the saturation was not reached, the data indicate the value $g_c/g_{ab} \approx 0.4$–$0.5$. A similar ratio was also found by Yadav *et al.* [39] using quantum chemistry methods and by fitting the high-field data of Ref. [35]. The corresponding $\delta$ puts the pseudospin angle $\alpha_S$ at relatively high values of about $\alpha_S \gtrsim 50^\circ$ [see Fig. 4(e)]. Adopting this estimate, we will try to identify a consistent parameter window.

Unfortunately, the present neutron experiment [38] could not directly resolve the orientation of the moments with respect to the $a$ axis, i.e., whether $\varphi = 0$ or 180°. The absence of this most conclusive evidence for the sign of the Kitaev interaction requires us to consider both possibilities.

We assume first FM $K < 0$ as obtained in two recent *ab initio* calculations of the exchange interactions in $RuCl_3$ [24,39]. Figure 3(c) gives a hint that the estimated $\alpha_S \gtrsim 50^\circ$ can be reached for small $\Gamma$ only. As seen in Fig. 3(d), by including small negative $\Gamma'$ that shifts the crossover towards negative $\Gamma$, the pseudospin direction may rotate even far above the $xy$ plane. Interestingly, the corresponding parameter regime $J \sim -\Gamma \sim -\Gamma' \sim 0.2|K|$ matches well the prediction by quantum chemistry calculations [39].

Now we analyze the AF $K > 0$ case, proposed for $RuCl_3$ in Refs. [13,38,40]. In this case, the zigzag order is obtained on the level of the two-parameter Kitaev-Heisenberg model [20] alone, and this simplicity makes the AF $K$ scenario particularly attractive. In the zigzag phase of the two-parameter model, the pseudospins point along the cubic $z$ axis leading to $\alpha_S \approx 35^\circ$. This can be reconciled with the experimental value $\alpha_M \approx 35^\circ$ only in a nearly cubic situation with a small trigonal distortion. Considering, however, the large anisotropy of the $g$ factors

discussed above and the resulting $\alpha_S \gtrsim 50^\circ$, it seems that the AF Kitaev interaction needs to be supplemented by other anisotropic interactions lifting the pseudospin considerably up. This scenario is addressed in Fig. 3(e). We have found that $\Gamma'$ does not influence $\alpha_S$ much so that we focus on the $\Gamma$ dependence. Since the AF $K$ zigzag phase becomes fragile if the other anisotropy terms are included, the model has to be additionally extended by $J_3$. Based on the data of Fig. 3(e), we may conclude that large negative $\Gamma$ comparable to $K$ is needed to obtain $\alpha_S \gtrsim 50^\circ$. It should be carefully checked if such a substantially extended model is still consistent with other experimental data, in particular with the spin excitation spectrum with only small gaps [13].

We would like to stress again that our analysis of $RuCl_3$ for both $K < 0$ and $K > 0$ heavily relied on the relative trigonal field strength $\Delta/\lambda$ inferred solely from the magnetization anisotropy in high magnetic fields. It is thus highly desirable to measure the complementary angle $\alpha_N$ by RXS and quantify $\Delta/\lambda$ more precisely, as suggested in the previous subsection. As discussed in Appendix C, measuring the anisotropy of $J = 3/2$ states by inelastic neutron scattering in single crystals would be also very helpful.

To summarize this section, in $Na_2IrO_3$, the measured moment direction [12] with $\varphi = 0^\circ$ well fixes the FM sign of the Kitaev interaction, and our analysis of its angle from the $ab$ plane suggests that $\Gamma \sim 0.3 - 0.5|K|$ coupling is present. Concerning $RuCl_3$, the current ambiguity in the angle $\varphi$ (0 or 180°) leaves open the issue of the sign of $K$. There is also an uncertainty in the trigonal field value $\Delta$; based so far on the $g$-factor anisotropy, we found that FM $K < 0$ with relatively small $\Gamma$ and $\Gamma'$ values would be consistent with the data, while the AF $K > 0$ situation requires large $\Gamma < 0$ couplings comparable to $K$.

## VII. CONCLUSIONS

We have investigated the ordered moment direction in the zigzag phases of the extended Kitaev-Heisenberg model for honeycomb lattice magnets. Our method analyzes the exact cluster ground states using a particular set of spin coherent states and as such fully accounts for the quantum fluctuations. The interplay among the various anisotropic interactions leads to a complex behavior of the ordered moment direction as a function of the model parameters. We have found substantial corrections to the results of a classical analysis that are important when quantifying the exchange interactions based on the experimental data.

We have pointed out that, away from the ideal cubic situation, the notion of the "ordered moment direction" has to be precisely specified. Assuming a trigonal field relevant to the layered honeycomb systems, we have derived relations among the directions of (i) the pseudospins entering the model Hamiltonian, (ii) the magnetic moments measured by neutron diffraction, and (iii) the moment direction as probed by resonant magnetic x-ray scattering. These relations and a combination of neutron and x-ray data should enable a reliable quantification of the trigonal field as well as the pseudospin direction in future experiments.

Using the above results, we have analyzed the currently available experimental data on $Na_2IrO_3$ and $RuCl_3$ and identified plausible parameter regimes in these compounds.

## ACKNOWLEDGMENTS

We would like to thank G. Jackeli, B. J. Kim, S. E. Nagler, and J. Rusnačko for helpful discussions. J.C. acknowledges support by Czech Science Foundation (GAČR) under Project No. GJ15-14523Y and MŠMT ČR under NPU II project CEITEC 2020 (Project No. LQ1601).

## APPENDIX A: COMPARISON OF NUMERICAL METHODS

As mentioned in the main text, the standard method to obtain the ordered moment direction using the ED ground state is to evaluate the spin-spin correlation matrix $\langle S^\alpha_{-\boldsymbol{Q}} S^\beta_{\boldsymbol{Q}} \rangle$ $(\alpha,\beta = x,y,z)$ at the ordering vector $\boldsymbol{Q}$ and to find its eigenvector corresponding to the largest eigenvalue. However, there are two main problems associated with this simple method, both emerging since the cluster ground state is a linear superposition of degenerate orderings where the individual orderings have equal weights.

(i) If there are several equivalent easy axis directions associated with the selected ordering vector $\boldsymbol{Q}$, they will be characterized by the same eigenvalue. This leads to a degenerate eigenspace and prevents us from resolving such directions. The most severe cases are those with a dominant Heisenberg interaction presented in Figs. 2(a) and 2(b). Here we have three degenerate easy axes $x$, $y$, and $z$ which makes the correlation matrix proportional to a unit matrix and thus isotropic. In the FM $K < 0$ zigzag situation shown in Fig. 2(d) and the entire middle phase in Fig. 3(a), two degenerate moment directions for a particular zigzag pattern (selected by $\boldsymbol{Q}$) are possible and the correlation matrix therefore just uncovers the softness of the $xy$ plane. Only after these two directions merge for a large enough $|\Gamma|$, the moment direction can be identified.

(ii) The zigzag pattern to be probed is selected by choosing the ordering vector $\boldsymbol{Q}$. In contrast to an infinite lattice, at a finite cluster this separation of the three zigzag directions is

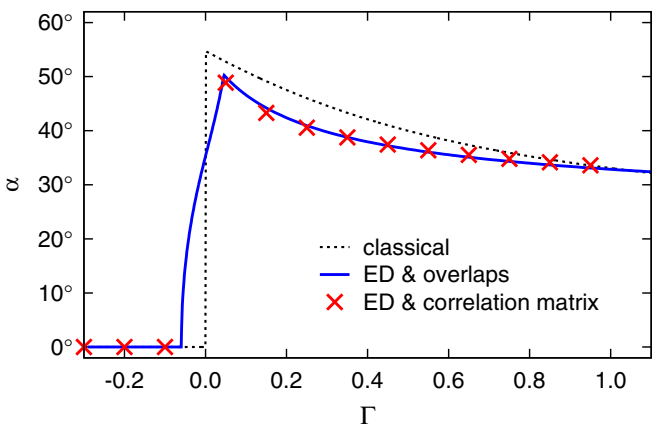


FIG. 5. Comparison of the angle $\alpha$ of the pseudospin direction to the $ab$ plane obtained using various methods. The parameters $K = -1$ and $J = J_3 = 0.2$ were used. The blue curve is identical to the one shown in Figs. 3(a)–3(d).

not perfect. The range of spin correlations is limited by the size of the cluster and the corresponding momentum space peaks become broad. The correlation matrix at given $\boldsymbol{Q}$ is thus "polluted" by small contributions of the two other zigzags in the ground state, that are associated with the remaining ordering vectors.

Our method introduced in Sec. IV does not suffer from the above problems and is able to handle all the situations encountered. This is due to the full resolution of the various degenerate orderings present in the cluster ground state by using a prescribed ordering pattern and by a construction of a full directional map.

If applicable, the standard method gives results very similar to our method. We demonstrate this in Fig. 5 that compares the two methods for the parameters $K = -1$, $J = J_3 = 0.2$ and varying $\Gamma$ used in Fig. 3. The slight deviations observed for $\Gamma > 0$ can be interpreted as a manifestation of the second problem discussed above.

## APPENDIX B: DERIVATION OF THE $L$-EDGE RXS OPERATOR

Resonant x-ray scattering is conceptually similar to the Raman light scattering, in a sense that both processes involve the intermediate states created and subsequently eliminated by incoming and outgoing photons. However, the nature of the intermediate states in these two cases is radically different: while the Raman light scattering involves intersite $d$-$d$ transitions, the x rays create the high-energy on-site $p$-$d$ transitions. As a result, the Raman light scattering probes intersite (two-magnon) spin flips, while the presence of a strong spin-orbit coupled $2p$-core hole in the RXS intermediate states makes single-ion spin flips a dominant magnetic scattering channel (see the recent review [41] and references therein for details).

A complex time dynamics of the intermediate states makes the x-ray-scattering process hard to analyze microscopically. However, as far as one is concerned with the low-energy excitations in Mott insulators, the problem of the intermediate states can be disentangled and cast in the form of frequency-independent phenomenological constants [42–44]. This results is an effective RXS operator formulated in terms of low-energy (orbital, spin, etc.) degrees of freedom alone. The form of this operator is dictated by symmetry. In essence, this approach is similar to that of Fleury and Loudon [45] widely used in the theories of Raman light scattering in quantum magnets.

While the RXS operator used in the main text follows from an underlying trigonal symmetry, the ratio between $f_{ab}$ and $f_c$ constants requires specific calculations. This can be easily done, with some routine modifications of the previous work for the case of tetragonal symmetry [46,47], as outlined below.

In cubic axes $x$,$y$, and $z$ (see Fig. 1), a dipolar $2p$ to $5d$ transition operator reads as

$$D = \varepsilon_x T_x + \varepsilon_y T_y + \varepsilon_z T_z, \tag{B1}$$

where $\varepsilon_{x,y,z}$ are the polarization factors, and $T_x = d^\dagger_{zx} p_z + d^\dagger_{xy} p_y$, $T_y = d^\dagger_{xy} p_x + d^\dagger_{yz} p_z$, $T_z = d^\dagger_{yz} p_y + d^\dagger_{zx} p_x$. Here and below, it is implied that $d$ and $p$ operators carry also the spin quantum numbers $(\uparrow, \downarrow)$ over which summation is taken.

In the quantization axes $a$,$b$, and $c$, suggested by the trigonal crystal field, this operator takes the following form:

$$D = \frac{1}{\sqrt{6}}(\varepsilon_a T_a + \varepsilon_b T_b + \varepsilon_c T_c), \tag{B2}$$

where

$$\begin{aligned} T_a &= (d^\dagger_0 + 2d^\dagger_{-1})p_1 + (d^\dagger_1 - d^\dagger_{-1})p_0 + (2d^\dagger_1 - d^\dagger_0)p_{-1}, \\ i\,T_b &= (-d^\dagger_0 + 2d^\dagger_{-1})p_1 + (d^\dagger_1 + d^\dagger_{-1})p_0 - (2d^\dagger_1 + d^\dagger_0)p_{-1}, \\ T_c &= \sqrt{2}\,(2d^\dagger_0 p_0 - d^\dagger_1 p_1 - d^\dagger_{-1} p_{-1}). \end{aligned} \tag{B3}$$

Here, the indices 0 and $\pm 1$ stand for the $l_c$ orbital quantum numbers of $d$ and $p$ electrons.

Within the above Fleury-Loudon-like approach to the x-ray-scattering problem, the effective RXS operator is given by $D^\dagger(\varepsilon')D(\varepsilon)$, and its part responsible for the magnetic scattering reads as $\hat{R} \propto i(\boldsymbol{\varepsilon} \times \boldsymbol{\varepsilon}') \cdot (\boldsymbol{T}^\dagger \times \boldsymbol{T})$.

Next, the core-hole operators $p$ in Eq. (B3) are expressed in terms of spin-orbit split $j = 1/2$ and $3/2$ eigenstates of the $2p$ level, resulting in two sets of $\boldsymbol{T}$ operators active in $L_2$ and $L_3$ edges, correspondingly. After "integrating out" these $2p_{\frac{1}{2}}$ and $2p_{\frac{3}{2}}$ operators, the product $(\boldsymbol{T}^\dagger \times \boldsymbol{T})$ becomes a simple quadratic form of $d$ operators. Finally, projecting this form onto a pseudospin doublet [given by Eqs. (14) and (15) of the main text], we arrive at the RXS operator $\hat{R} \propto i f_{ab}(P_a S_a + P_b S_b) + i f_c P_c S_c$, with the $f$ factors shown in the main text. Via the pseudospin wave functions, the RXS $f$ factors are sensitive to a trigonal field strength.

## APPENDIX C: DETERMINATION OF THE TRIGONAL FIELD FROM $J = 3/2$ MAGNETIC EXCITATION SPECTRA

Under spin-orbit coupling $\lambda$ and trigonal crystal field $\Delta$, $t_{2g}$-hole states split into three levels $A$, $B$, and $C$ [see Fig. 6(a)]. The $A$ level hosts a Kramers pseudospin one-half (corresponding to $J = 1/2$ in the cubic limit), with the wave functions

$$|A_+\rangle = +\sin\vartheta\,|0,\uparrow\rangle - \cos\vartheta\,|+1,\downarrow\rangle, \tag{C1}$$

$$|A_-\rangle = -\sin\vartheta\,|0,\downarrow\rangle + \cos\vartheta\,|-1,\uparrow\rangle, \tag{C2}$$

as were given by Eqs. (14) and (15) of the main text. The upper Kramers doublets $B$ and $C$ are derived from the spin-orbit $J = 3/2$ quartet. The former correspond to pure $J_c = \pm 3/2$ states of $J = 3/2$ moment:

$$|B_+\rangle = |+1,\uparrow\rangle, \tag{C3}$$

$$|B_-\rangle = |-1,\downarrow\rangle, \tag{C4}$$

while the $C$ level wave functions are given by

$$|C_+\rangle = \cos\vartheta\,|0,\uparrow\rangle + \sin\vartheta\,|+1,\downarrow\rangle, \tag{C5}$$

$$|C_-\rangle = \cos\vartheta\,|0,\downarrow\rangle + \sin\vartheta\,|-1,\uparrow\rangle, \tag{C6}$$

corresponding to $J_c = \pm 1/2$ states of the $J = 3/2$ quartet in the cubic limit, and containing some admixture of

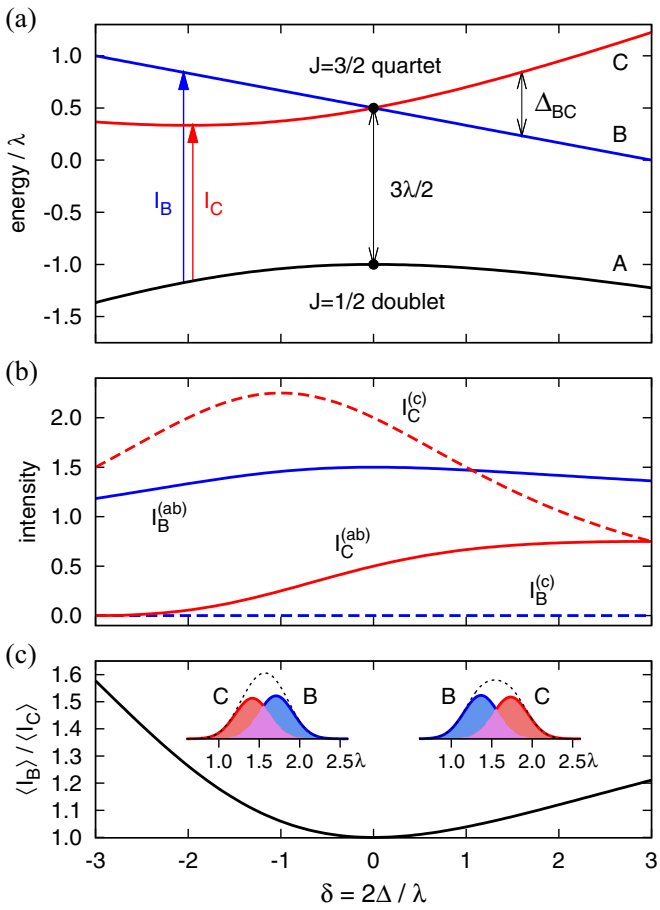


FIG. 6. (a) Level structure of a $d^5(t_{2g})$ ion upon trigonal field splitting characterized by $\delta = 2\Delta/\lambda$ (hole picture). (b) Intensities of the magnetic transitions $A \to B$ and $A \to C$ for the $ab$-plane and $c$-axis components of the dynamical spin structure factor as given by Eqs. (C11) and (C13). (c) Ratio of the powder-averaged intensities. The insets show the broadened (HWHM $= \frac{1}{4}\lambda$) peak structure assuming $\delta = -1$ (left) and $\delta = +1$ (right), respectively.

the original $J = 1/2$ doublet at finite $\Delta$. The energies of these states are $E_{A,C}/\lambda = \frac{1}{4}[\mp\sqrt{8+(1+\delta)^2} - 1] + \frac{1}{12}\delta$ and $E_B/\lambda = \frac{1}{2} - \frac{1}{6}\delta$.

Transitions from the ground-state $A$ level to $B$ and $C$ states are magnetically active; their spectral weights in the dynamical spin structure factor are determined by matrix elements of the magnetic moment $\boldsymbol{M} = 2\boldsymbol{s} - \boldsymbol{l}$:

$$\mp\langle B_\pm|M_a|A_\pm\rangle = \frac{1}{i}\langle B_\pm|M_b|A_\pm\rangle = \cos\vartheta + \frac{1}{\sqrt{2}}\sin\vartheta, \tag{C7}$$

$$\pm\langle C_\mp|M_a|A_\pm\rangle = \frac{1}{i}\langle C_\mp|M_b|A_\pm\rangle = \frac{1}{2}(s_{2\vartheta} + \sqrt{2}c_{2\vartheta})\,. \tag{C8}$$

Out-of-plane moment $M_c$ matrix elements between $A$ and $B$ vanish (independent of the spin-orbit mixing angle $\vartheta$), while

$$\langle C_\pm|M_c|A_\pm\rangle = \tfrac{3}{2}s_{2\vartheta}. \tag{C9}$$

In the magnetic excitation spectra, a transition $A \to B$ gives a peak at the energy

$$E_B - E_A = \frac{\lambda}{4}[\sqrt{8+(1+\delta)^2} + 3 - \delta], \tag{C10}$$

with the following intensities for different components of the dynamical spin structure factor:

$$I_B = \begin{cases} \frac{1}{4}(3 + c_{2\vartheta} + 2\sqrt{2}s_{2\vartheta}) & (ab \text{ plane}) \\ 0 & (c \text{ axis}) \end{cases}. \tag{C11}$$

The second transition $A \to C$ is peaked at the energy

$$E_C - E_A = \frac{\lambda}{2}\sqrt{8+(1+\delta)^2} \tag{C12}$$

and has the intensity

$$I_C = \begin{cases} \frac{1}{4}(s_{2\vartheta} + \sqrt{2}c_{2\vartheta})^2 & (ab \text{ plane}) \\ \frac{9}{4}s_{2\vartheta}^2 & (c \text{ axis}) \end{cases}. \tag{C13}$$

The $B$ and $C$ peaks are separated by $\Delta_{BC}/\lambda = \frac{1}{4}[\sqrt{8+(1+\delta)^2} - 3 + \delta]$; at small trigonal splitting $\Delta \ll \lambda$, this can be approximated as $\Delta_{BC} \approx \frac{2}{3}\Delta$. At positive (negative) $\Delta$, the $B$ peak position is lower (higher) than that of the $C$ peak [see Fig. 6(a)].

Figure 6(b) shows that the intensities of both transitions are highly anisotropic with respect to $ab$-plane and $c$-axis polarizations, with the opposite behavior of $B$ and $C$ contributions. The out-of-plane response is due to the $C$ transition exclusively, while the $B$ peak dominates the $ab$-plane intensity. This should enable one to distinguish them and determine thereby both the sign and value of trigonal field parameter $\delta$ from single-crystal spin-polarized neutron-scattering data.

On the other hand, the powder averaged intensities of $B$ and $C$ peaks are nearly the same for realistic values of $\delta$ [see Fig. 6(c)]. Even at $|\delta| = 1$, the two peaks may overlap to give a single broad line, leaving an ambiguity in the sign of parameter $\delta$.

[1] N. F. Mott, *Metal-Insulator Transitions* (Taylor and Francis, London, 1974).
[2] M. Imada, A. Fujimori, and Y. Tokura, Rev. Mod. Phys. **70**, 1039 (1998).
[3] J. B. Goodenough, *Magnetism and the Chemical Bond* (Interscience, New York, 1963).
[4] K. I. Kugel and D. I. Khomskii, Sov. Phys. Usp. **25**, 231 (1982).
[5] G. Khaliullin and S. Maekawa, Phys. Rev. Lett. **85**, 3950 (2000).
[6] G. Khaliullin, Prog. Theor. Phys. Suppl. **160**, 155 (2005).
[7] A. Abragam and B. Bleaney, *Electron Paramagnetic Resonance of Transition Ions* (Clarendon, Oxford, 1970).
[8] G. Khaliullin, W. Koshibae, and S. Maekawa, Phys. Rev. Lett. **93**, 176401 (2004).

[9] G. Jackeli and G. Khaliullin, Phys. Rev. Lett. **102**, 017205 (2009).

[10] A. Kitaev, Ann. Phys. **321**, 2 (2006).

[11] J. G. Rau, E. K.-H. Lee, and H.-Y. Kee, Annu. Rev. Condens. Matter Phys. **7**, 195 (2016).

[12] S. H. Chun, J.-W. Kim, Jungho Kim, H. Zheng, C. C. Stoumpos, C. D. Malliakas, J. F. Mitchell, K. Mehlawat, Y. Singh, Y. Choi, T. Gog, A. Al-Zein, M. Moretti Sala, M. Krisch, J. Chaloupka, G. Jackeli, G. Khaliullin, and B. J. Kim, Nat. Phys. **11**, 462 (2015).

[13] A. Banerjee, C. A. Bridges, J.-Q. Yan, A. A. Aczel, L. Li, M. B. Stone, G. E. Granroth, M. D. Lumsden, Y. Yiu, J. Knolle, S. Bhattacharjee, D. L. Kovrizhin, R. Moessner, D. A. Tennant, D. G. Mandrus, and S. E. Nagler, Nat. Mater. **15**, 733 (2016).

[14] K. W. Plumb, J. P. Clancy, L. J. Sandilands, V. V. Shankar, Y. F. Hu, K. S. Burch, H.-Y. Kee, and Y.-J. Kim, Phys. Rev. B **90**, 041112(R) (2014).

[15] J. Chaloupka, G. Jackeli, and G. Khaliullin, Phys. Rev. Lett. **105**, 027204 (2010).

[16] V. M. Katukuri, S. Nishimoto, V. Yushankhai, A. Stoyanova, H. Kandpal, S. Choi, R. Coldea, I. Rousochatzakis, L. Hozoi, and J. van den Brink, New J. Phys. **16**, 013056 (2014).

[17] J. G. Rau, E. K.-H. Lee, and H.-Y. Kee, Phys. Rev. Lett. **112**, 077204 (2014).

[18] J. G. Rau and H.-Y. Kee, arXiv:1408.4811.

[19] J. Chaloupka and G. Khaliullin, Phys. Rev. B **92**, 024413 (2015).

[20] J. Chaloupka, G. Jackeli, and G. Khaliullin, Phys. Rev. Lett. **110**, 097204 (2013).

[21] I. Kimchi and Y.-Z. You, Phys. Rev. B **84**, 180407(R) (2011).

[22] S. K. Choi, R. Coldea, A. N. Kolmogorov, T. Lancaster, I. I. Mazin, S. J. Blundell, P. G. Radaelli, Y. Singh, P. Gegenwart, K. R. Choi, S.-W. Cheong, P. J. Baker, C. Stock, and J. Taylor, Phys. Rev. Lett. **108**, 127204 (2012).

[23] Y. Yamaji, Y. Nomura, M. Kurita, R. Arita, and M. Imada, Phys. Rev. Lett. **113**, 107201 (2014).

[24] S. M. Winter, Y. Li, H. O. Jeschke, and R. Valentí, Phys. Rev. B **93**, 214431 (2016).

[25] Y. Sizyuk, P. Wölfle, and N. B. Perkins, Phys. Rev. B **94**, 085109 (2016).

[26] A. Auerbach, *Interacting Electrons and Quantum Magnetism* (Springer, New York, 1994).

[27] For a discussion of the order-from-disorder phenomena in frustrated spin systems, see A. M. Tsvelik, *Quantum Field Theory in Condensed Matter Physics* (Cambridge University, Cambridge, England, 1995), Chap. 17, and references therein.

[28] G. Jackeli and A. Avella, Phys. Rev. B **92**, 184416 (2015).

[29] G. Khaliullin, Phys. Rev. B **64**, 212405 (2001).

[30] Z. Nussinov and J. van den Brink, Rev. Mod. Phys. **87**, 1 (2015).

[31] However, the separation of the individual zigzag chain directions is an order-from-disorder effect, since a linear combination of different zigzag patterns is a classical ground state as well.

[32] S. Bhattacharjee, S.-S. Lee, and Y. B. Kim, New J. Phys. **14**, 073015 (2012).

[33] B. J. Kim, H. Ohsumi, T. Komesu, S. Sakai, T. Morita, H. Takagi, and T. Arima, Science **323**, 1329 (2009).

[34] Y. Kubota, H. Tanaka, T. Ono, Y. Narumi, and K. Kindo, Phys. Rev. B **91**, 094422 (2015).

[35] R. D. Johnson, S. C. Williams, A. A. Haghighirad, J. Singleton, V. Zapf, P. Manuel, I. I. Mazin, Y. Li, H. O. Jeschke, R. Valentí, and R. Coldea, Phys. Rev. B **92**, 235119 (2015).

[36] Y. Singh and P. Gegenwart, Phys. Rev. B **82**, 064412 (2010).

[37] H. Gretarsson, J. P. Clancy, X. Liu, J. P. Hill, E. Bozin, Y. Singh, S. Manni, P. Gegenwart, J. Kim, A. H. Said, D. Casa, T. Gog, M. H. Upton, H.-S. Kim, J. Yu, V. M. Katukuri, L. Hozoi, J. van den Brink, and Y.-J. Kim, Phys. Rev. Lett. **110**, 076402 (2013).

[38] H. B. Cao, A. Banerjee, J.-Q. Yan, C. A. Bridges, M. D. Lumsden, D. G. Mandrus, D. A. Tennant, B. C. Chakoumakos, and S. E. Nagler, Phys. Rev. B **93**, 134423 (2016).

[39] R. Yadav, N. A. Bogdanov, V. M. Katukuri, S. Nishimoto, J. van den Brink, and L. Hozoi, arXiv:1604.04755.

[40] H.-S. Kim, Vijay Shankar V., A. Catuneanu, and H.-Y. Kee, Phys. Rev. B **91**, 241110(R) (2015).

[41] L. J. P. Ament, M. van Veenendaal, T. P. Deveraux, J. P. Hill, and J. van den Brink, Rev. Mod. Phys. **83**, 705 (2011).

[42] L. J. P. Ament and G. Khaliullin, Phys. Rev. B **81**, 125118 (2010).

[43] M. W. Haverkort, Phys. Rev. Lett. **105**, 167404 (2010).

[44] L. Savary and T. Senthil, arXiv:1506.04752.

[45] P. A. Fleury and R. Loudon, Phys. Rev. **166**, 514 (1968).

[46] L. J. P. Ament, G. Khaliullin, and J. van den Brink, Phys. Rev. B **84**, 020403(R) (2011).

[47] J. Kim, D. Casa, M. H. Upton, T. Gog, Y.-J. Kim, J. F. Mitchell, M. van Veenendaal, M. Daghofer, J. van den Brink, G. Khaliullin, and B. J. Kim, Phys. Rev. Lett. **108**, 177003 (2012).